Calibration of Suomi national polar-orbiting partnership advanced technology microwave sounder

Fuzhong Weng,[1] Xiaolei Zou,[2] Ninghai Sun,[3] Hu Yang,[3] Miao Tian,[3]
William J. Blackwell,[4] Xiang Wang,[2,5] Lin Lin,[6] and Kent Anderson[7]

[1]   The Suomi National Polar-Orbiting Partnership (NPP) satellite was launched on 28 October 2011 and carries the Advanced Technology Microwave Sounder (ATMS) on board. ATMS is a cross-track scanning instrument observing in 22 channels at frequencies ranging from 23 to 183 GHz, permitting the measurements of the atmospheric temperature and moisture under most weather conditions. In this study, the ATMS radiometric calibration algorithm used in the operational system is first evaluated through independent analyses of prelaunch thermal vacuum data. It is found that the ATMS peak nonlinearity for all the channels is less than 0.5 K, which is well within the specification. For the characterization of the ATMS instrument sensitivity or noise equivalent differential temperatures (NEDT), both standard deviation and Allan variance of warm counts are computed and compared. It is shown that NEDT derived from the standard deviation is about three to five times larger than that from the Allan variance. The difference results from a nonstationary component in the standard deviation of warm counts. The Allan variance is better suited than the standard deviation for describing NEDT. In the ATMS sensor brightness temperature data record (SDR) processing algorithm, the antenna gain efficiencies of main beam, cross-polarization beam, and side lobes must be derived accurately from the antenna gain distribution function. However, uncertainties remain in computing the efficiencies at ATMS high frequencies. Thus, ATMS antenna brightness temperature data records (TDR) at channels 1 to 15 are converted to SDR with the actual beam efficiencies whereas those for channels 16 to 22 are only corrected for the near-field sidelobe contributions. The biases of ATMS SDR measurements to the simulations are consistent between GPS RO and NWP data and are generally less than 0.5 K for those temperature-sounding channels where both the forward model and input atmospheric profiles are reliable.

Citation: Weng, F., X. Zou, N. Sun, H. Yang, M. Tian, W. J. Blackwell, X. Wang, L. Lin, and K. Anderson (2013), Calibration of Suomi national polar-orbiting partnership advanced technology microwave sounder, *J. Geophys. Res. Atmos.*, *118*, 11,187–11,200, doi:10.1002/jgrd.50840.

1.   Introduction

[2]   On 28 October 2011, the Suomi National Polar-Orbiting Partnership (SNPP) satellite was successfully launched into an orbit which has an inclination angle of 98.7° to the equator

[1]NOAA Center for Satellite Applications and Research, College Park, Maryland, USA.
[2]Department of EOAS, Florida State University, Tallahassee, Florida, USA.
[3]ESSIC, University of Maryland, College Park, Maryland, USA.
[4]Sensor Technology and System Applications, MIT Lincoln Laboratory, Lexington, Massachusetts, USA.
[5]Center of Data Assimilation for Research and Application, Nanjing University of Information Science and Technology, Nanjing, China.
[6]Earth Resources Technology, Inc., Laurel, Maryland, USA.
[7]Northrop Grumman Electronic System (NGES), Redondo Beach, California, USA.

Corresponding author: F. Weng, NOAA Center for Satellite Applications and Research, 5830 University Research Court, College Park, Maryland 20740, USA. (Fuzhong.Weng@noaa.gov)

and is 824 km above the Earth. On board the SNPP satellite, the Advanced Technology Microwave Sounder (ATMS) is a cross-track scanning instrument and has 22 channels at frequencies ranging from 23 to 183 GHz for profiling the atmospheric temperature and moisture under clear and cloudy conditions. Table 1 summarizes the general information of the ATMS 22 channels. So far, ATMS data including calibration, geolocation, telemetry, and housekeeping have been processed at the ground Interface Data and Processing Segment (IDPS) since the SNPP launch. ATMS data was declared at the provisional maturity level on 3 January 2013. The ATMS antenna brightness temperature data record (TDR) and sensor data record (SDR) have been distributed to the user community from NOAA's Comprehensive Large Array-Data Stewardship Systems (CLASS) for various applications.

[3]   Preliminary investigations of ATMS data quality and its potential applications were discussed elsewhere. *Weng et al.* [2013] provided ATMS channel specifications and bias characteristics and illustrated a capability of ATMS to provide

Table 1. Requirements and Characteristics of the ATMS 22 Channels, Including the Channel Weighting Function Peaks at a US Standard Atmospheric Condition

Channel	Center Frequency (GHz)	Maximum Bandpass Width (GHz)	Quasi Polarization	Accuracy (K)	NEΔT (K)	Static Beamwidth (deg)	Weighting Function Peak (hPa)
1	23.8	0.27	QV	1.00	0.70	5.2	Window
2	31.4	0.18	QV	1.00	0.80	5.2	Window
3	50.3	0.18	QH	0.75	0.90	2.2	Window
4	51.76	0.40	QH	0.75	0.70	2.2	950
5	52.8	0.40	QH	0.75	0.70	2.2	850
6	53.596±0.115	0.17	QH	0.75	0.70	2.2	700
7	54.4	0.40	QH	0.75	0.70	2.2	400
8	54.94	0.40	QH	0.75	0.70	2.2	250
9	55.5	0.33	QH	0.75	0.70	2.2	200
10	57.29	0.33	QH	0.75	0.75	2.2	100
11	57.29±0.217	0.078	QH	0.75	1.20	2.2	50
12	57.29±0.322±0.048	0.036	QH	0.75	1.20	2.2	25
13	57.29±0.322±0.022	0.016	QH	0.75	1.50	2.2	10
14	57.29±0.322±0.010	0.008	QH	0.75	2.40	2.2	5
15	57.29±0.322±0.0045	0.003	QH	0.75	3.60	2.2	2
16	88.2	2.0	QV	1.00	0.50	2.2	Window
17	165.5	3.0	QH	1.00	0.60	1.1	Window
18	183.31±7.0	2.0	QH	1.00	0.80	1.1	800
19	183.31±4.5	2.0	QH	1.00	0.80	1.1	700
20	183.31±3.0	1.0	QH	1.00	0.80	1.1	500
21	183.31±1.8	1.0	QH	1.00	0.80	1.1	400
22	183.31±1.0	0.5	QH	1.00	0.90	1.1	300

more detailed thermal structures of tropical cyclones than its heritage predecessors. The scan angle-dependent features in the ATMS antenna brightness temperatures were analyzed using its pitch-over maneuver data [*Weng et al.*, 2013]. It was found that the contributions of spacecraft radiation through the near-field sidelobes or the emission from the flat reflector (E. Kim et al., S-NPP ATMS instrument pre-launch and on-orbit performance evaluation, submitted to *Journal of Geophysical Research: Atmospheres*, 2013) are significant and result in the scan angle-dependent ATMS antenna brightness temperatures. The scan angle biases at ATMS upper level sounding channels were further quantified by using the Global Positioning System (GPS) Radio Occultation (RO) data as inputs to the radiative transfer model [*Zou et al.*, 2013]. Today, ATMS radiance data are successfully assimilated into the NOAA global and regional

forecast models and the ECMWF global forecast system. The impacts of the ATMS data assimilation on global and regional forecasts can be found in the studies of *Bormann et al.* [2013] and *Zou et al.* [2013].

[4] This work describes in details the ATMS calibration process from raw data records to the antenna brightness temperatures and sensor data records. In section 2, the ATMS instrument characteristics are presented. In section 3, the ATMS radiometric calibration procedure is described with respect to the two-point calibration algorithm. Section 4 presents the methodology for ATMS noise sensitivity characterization. The algorithms of ATMS TDR to SDR conversion are highlighted in section 5. Independent on-orbit SDR accuracy assessments using either the NCEP GFS 6 h forecasts or the collocated GPS RO as inputs to the NWP Community Radiative Transfer Model (CRTM) are given in
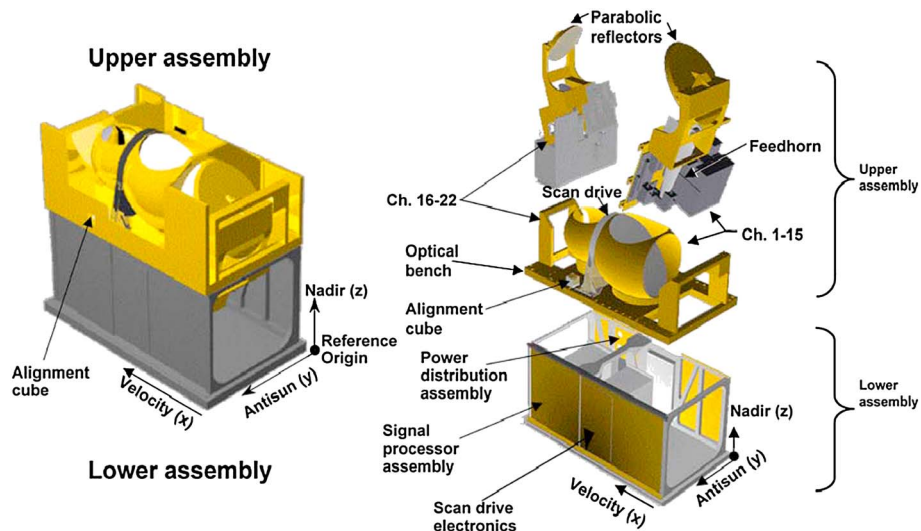
Figure 1. Schematic diagram of ATMS instrument layout [*JPSS ATMS ATBD*, 2011].
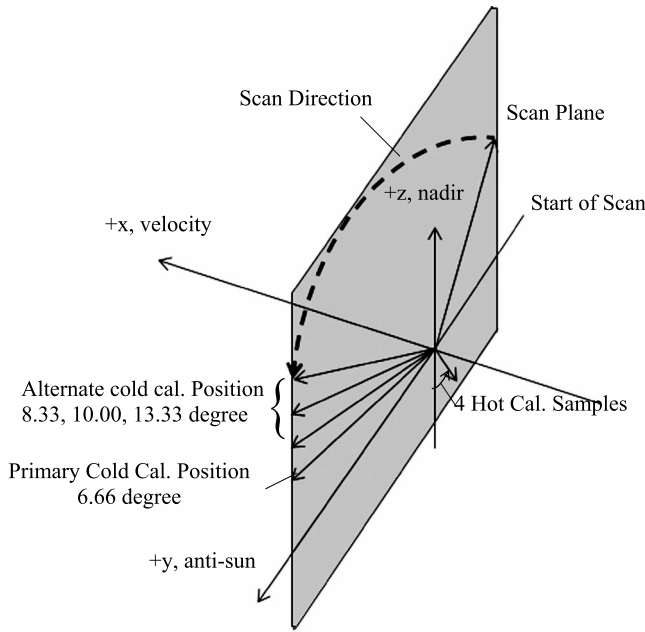
Figure 2. ATMS scan cycle during which 96 Earth views, four cold and four warm calibrations are made. The angle at each cold calibration position is defined with respect to the *y* axis of the anti-Sun direction.

section 6. Section 7 summarizes the overall ATMS performances from our calibration and validation research.

2. Instrument Description

[5] ATMS scan angle ranges within ±52.725° from the nadir direction. It has 22 channels with the first 16 channels primarily for temperature soundings from the surface to about 1 hPa (~45 km) and the remaining six channels for humidity soundings in the troposphere from the surface to about 200 hPa (~15 km). The ATMS channels 3–16 have a beam width of 2.2°, which is smaller than that of the corresponding AMSU-A channels 3–16. However, the beam width of the ATMS channels 1–2 is 5.2°, which is much larger than that of the corresponding AMSU-A channels 1–2. The ATMS channels 17–22 have a beam width of 1.1°, which is the same as that of the AMSU-B and MHS channels.

[6] Figure 1 shows a schematic diagram of the assembling position of ATMS on the SNPP platform. The antenna reflectors rotate counterclockwise relative to the spacecraft direction of motion (i.e., the *x* direction) to complete three revolutions in 8 s. The scan mechanism is synchronized to the spacecraft clock with a "sync" pulse every 8 s (i.e., at every third revolution). As shown in Figure 2, each ATMS scan cycle is divided into three segments. In the first segment, the earth is viewed at 96 different scan angles, which are distributed symmetrically around the nadir direction. Such 96 ATMS field-of-view (FOV) samples are taken "on the fly" with each FOV sample representing the mid-point of a brief sampling interval of about 18 ms. With a scan rate of 61.6° per second, the angular sampling interval is 1.11°. Therefore, the angular range between the first and last (i.e., 96th) sample centroids is 105.45° (i.e., ±52.725°

relative to nadir). As soon as completing one scan line, the antenna accelerates and moves to a position that points to an unobstructed view of space (i.e., between the Earth's limb and the spacecraft horizon). Then it resumes the same slow scan speed as it scans across the Earth scenes. In this period, four consecutive cold calibration measurements are taken. Next, the antenna accelerates again to the zenith direction where the blackbody target is located, and takes four consecutive warm calibration measurements with the same slow scan speed. Finally, it accelerates back to the starting position and then slows down to the normal scan speed for continuing the next scan cycle. More details of the ATMS scan mechanism can be found in [*JPSS ATMS ATBD*, 2011].

[7] ATMS has two sets of receiving antenna and reflector. One serves for channels 1–15 with frequencies below 60 GHz and another serves for channels 16–22 with frequencies above 60 GHz. Each receiving antenna is paired with a plane reflector mounted on a scan axis at a 45° tilt angle so that the incoming radiation is reflected from a direction perpendicular to the scan axis into a direction along the scan axis (i.e., a 90° reflection) (see Figure 3). With the scan axis oriented in the along-track direction, this results in a cross-track scan pattern. The reflected radiation is focused by a stationary parabolic reflector onto a dichroic plate, and then either reflected to or passed through to a feedhorn. Each aperture/reflector serves two frequency bands for a total of four bands.

3. ATMS Radiometric Calibration

[8] ATMS antenna/receiver system measures the radiation from two calibration sources during every scan cycle. The first source is the well-known cosmic background radiation. This source (often called as "cold space") is viewed
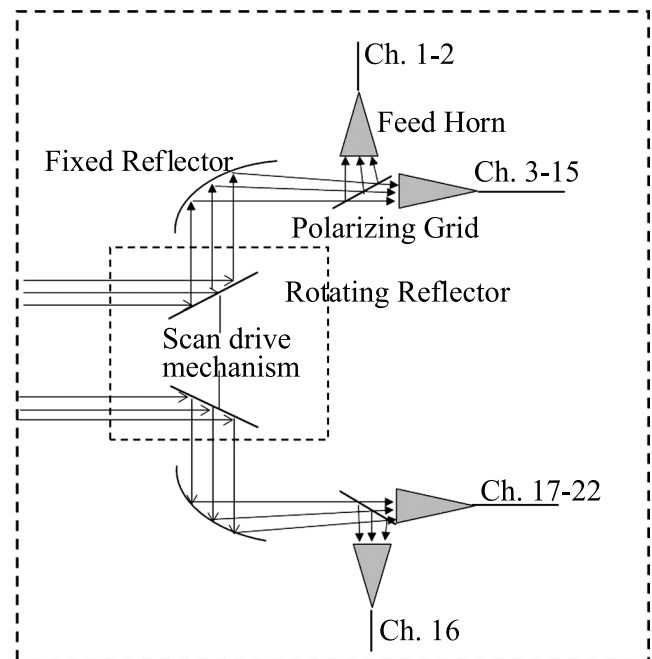

Figure 3. Schematic diagram of ATMS antenna subsystem. The top portion shows the antenna subsystem for K/Ka and V bands whereas the lower portion is for W/G bands.
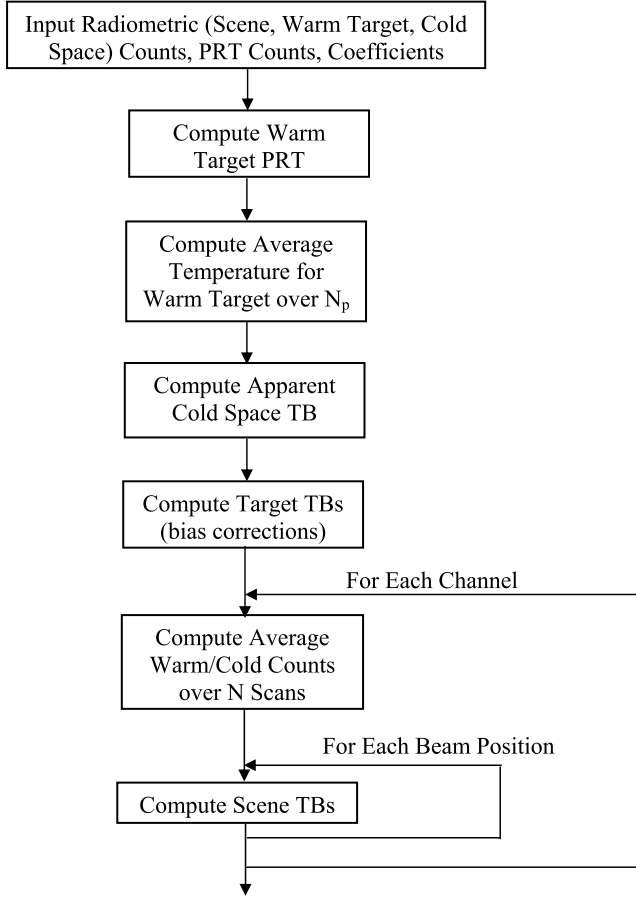
Input Radiometric (Scene, Warm Target, Cold Space) Counts, PRT Counts, Coefficients

↓

Compute Warm Target PRT

↓

Compute Average Temperature for Warm Target over N_p

↓

Compute Apparent Cold Space TB

↓

Compute Target TBs (bias corrections)

↓ For Each Channel

Compute Average Warm/Cold Counts over N Scans

↓ For Each Beam Position

Compute Scene TBs

Figure 4. ATMS radiometric calibration flow chart corresponding to the process in Suomi NPP ground processing system. N_p is the number of measurements made at every scan line for warm and cold targets. TB denotes the brightness temperature in Kelvin.

immediately after the Earth has been scanned. The second source is an internal blackbody calibration target (often called as "warm load"), whose physical temperature is the same as the instrument internal ambient temperature. This warm source is viewed immediately after the space calibration view. Every scan cycle (8/3 s) contains the above three consecutive views: Earth scene, cold space, and warm calibration measurements. Such a thorough radiometer calibration procedure allows the most impacts from ATMS system gain variations to be automatically eliminated since the two calibration measurements used for computing the gain involve the same optical and electrical signal paths as that of the Earth scene measurements. Thus, ATMS has an advantage over those calibration systems using switched internal calibration sources, which yields the calibration measurements having slightly different signal paths than that of the Earth scene measurements.

[9] The two calibration measurements are used to accurately determine the so-called radiometer transfer function, which converts the measured digitized output (i.e., counts) to a radiometric brightness temperature [*JPSS ATMS ATBD*, 2011]. The ATMS radiometric calibration flow chart corresponding to the interface data processing system (IDPS) is provided in Figure 4. The current ATMS antenna

brightness temperature is obtained through the following equation:

$$
\begin{aligned}
T_{b,ch} = T_{b,ch}^w &+ \frac{C_{ch}^s - \overline{C_{ch}^w}}{\overline{C_{ch}^w} - \overline{C_{ch}^c}}\left(T_{b,ch}^w - T_{b,ch}^c\right) \\
&+ \frac{1}{4}\mu\left(1 - 4(x - 0.5)^2\right)\left(T_{b,ch}^w - T_{b,ch}^c\right)^2 \\
\equiv T_{b,ch}^w &+ \left(\overline{G_{ch}}\right)^{-1}\left(C_{ch}^s - \overline{C_{ch}^w}\right) + Q_{ch}
\end{aligned}
\tag{1}
$$

where Q_{ch} is the channel based (subscript, ch) quadratic correction term; μ is a free parameter defined in [*Mo*, 1999]; x is a function of the cold space temperature and calibration warm target temperatures (see Appendix A); $\overline{G_{ch}}(i)$ is the averaged gain function at the ith scan line, defined via

$$
\overline{C_{ch}^w}(i) = \sum_{k=i-N_s}^{i+N_s}\sum_{j=1}^{4} W_{k-i}C_{ch}^w(k,j)
\tag{2a}
$$

$$
\overline{C_{ch}^c}(i) = \sum_{k=i-N_s}^{i+N_s}\sum_{j=1}^{4} W_{k-i}C_{ch}^c(k,j)
\tag{2b}
$$

$$
\overline{G_{ch}}(i) = \frac{\overline{C_{ch}^w}(i) - \overline{C_{ch}^c}(i)}{\overline{T_{b,ch}^w}(i) - T_{b,ch}^c}
\tag{2c}
$$

[10] The other terms used in equations (1), (2a), (2b), and (2c) are that $T_{b,ch}^w$ is the warm load brightness temperature; C_{ch}^s is the scene count; $C_{ch}^w(i,j)$ is the warm load count at the ith scan line of the jth sample, $C_{ch}^c(i,j)$ is the cold space count at the ith scan line of the jth sample; W_i is the weighting coefficient obtained from using either a triangular or boxcar function for averaging the warm and cold counts of $(2N_s + 1)$ consecutive scan lines; and $G_{ch}(i)$ is the calibration gain at the ith scan line. Overbar on each variable represents an average over a number of scan lines.

[11] Calculations of the averaged warm load and cold space counts, $\overline{C_{ch}^w}(i)$ and $\overline{C_{ch}^c}(i)$, depend on the weighting coefficients as well as the number of scan line involved in the averaging (i.e., $2N_s + 1$). For example, with the application of a triangular function, the weighting coefficients of all ATMS channels for the kth scan line are averaged as follows:

$$
W_k = \frac{1}{N_s + 1}\left(1 - \frac{|k|}{N_s + 1}\right)
\tag{3}
$$

[12] Other details of the radiometric calibration from radiance to brightness temperature can be found in Appendix A.

[13] The nonlinearity parameter, Q_{ch} in equation (1) is estimated using the prelaunch thermal vacuum (TVAC) data sets that are measured at different scene temperatures. For SNPP ATMS TVAC test, the scene temperature is typically measured between 93 and 330 K. However, for ATMS on-orbit calibration, the cold calibration temperature is approximately 3 K. Thus, the nonlinearity value must be estimated by extrapolating the TVAC data down to 3 K. In general, the nonlinear parameter Q_{ch} can be expressed as a quadratic function of scene temperature ($T_{b,ch}$) as

$$
Q_{ch} = b_{0,ch} + b_{1,ch}T_{b,ch} + b_{2,ch}\left(T_{b,ch}\right)^2
\tag{4}
$$

Table 2. An Example Set of Quadratic Coefficients From Fitting the Nonlinearity Data Measured for ATMS CP RC1 at +5°C[a]

	NGES			STAR		
Chan.	b_0	b_1	b_2 (× 10^{-4})	b_0	b_1	b_2 (× 10^{-4})
1	−0.8810	0.0072	−0.1370	−0.8814	0.0072	−0.1371
2	−0.7010	0.0047	−0.0691	−0.7015	0.0047	−0.0692
3	−0.1610	0.0038	−0.1080	−0.1608	0.0038	−0.1079
4	−0.2970	0.0055	−0.1480	−0.2975	0.0055	−0.1481
5	−0.2870	0.0054	−0.1460	−0.2874	0.0054	−0.1461
6	−0.0780	0.0027	−0.0772	−0.0787	0.0027	−0.0774
7	−0.0666	0.0027	−0.0785	−0.0666	0.0027	−0.0785
8	−0.2360	0.0049	−0.1370	−0.2363	0.0049	−0.1371
9	0.0479	0.0007	−0.0224	0.0475	0.0007	−0.0225
10	−0.2150	0.0050	−0.1430	−0.2157	0.0050	−0.1432
11	−0.1440	0.0043	−0.1250	−0.1441	0.0043	−0.1250
12	−0.1680	0.0044	−0.1280	−0.1680	0.0044	−0.1280
13	−0.1520	0.0040	−0.1120	−0.1517	0.0040	−0.1119
14	0.0953	0.0013	−0.0485	0.0927	0.0014	−0.0492
15	−0.0321	0.0029	−0.0924	−0.0341	0.0030	−0.0930
16	−1.5100	0.0110	−0.1790	−1.5081	0.0110	−0.1786
17	−0.4870	0.0080	−0.2080	−0.4838	0.0080	−0.2072
18	−0.2270	0.0057	−0.1600	−0.2243	0.0057	−0.1594
19	−0.2290	0.0059	−0.1660	−0.2264	0.0058	−0.1654
20	−0.3240	0.0071	−0.1960	−0.3201	0.0071	−0.1951
21	−0.2280	0.0060	−0.1660	−0.2223	0.0059	−0.1646
22	−0.2940	0.0070	−0.1950	−0.2899	0.0070	−0.1939

[a]The fitting coefficients are based on data within the scene temperature of 93 K to 330 K. For each RC, the mean quadratic coefficients are derived at three separate instrument temperature conditions (+20°C, +5°C, and −10°C).

where $b_{i,ch}$ ($i = 0, 1, 2$; $ch = 1, \ldots, 22$) are unknown coefficients. The values of them can be obtained by applying a least square fit to the TVAC data measured within the temperature range of 93 to 330 K. Then, by applying these coefficients back into equation (4), one can compute Q_{ch} for all scene temperatures within and beyond the range of 93 to 330 K. One example of $b_{i,ch}$ is given in Table 2. Figure 5 presents an example of the $Q_{ch}(T_{b,ch})$ of ATMS channel 1, obtained from applying the TVAC measured scene temperatures for cold plate (CP) at 5°C from redundancy configuration 1 (RC1). The peak nonlinearity is located near 170 K, which is about in the middle between 3 and 330 K. Table 3 provides the maximum nonlinearity, $Q_{ch}^{max} = \frac{1}{4}\mu\left(T_{b,ch}^w - T_{b,ch}^c\right)^2$, for a scene temperature range between 3 K and 276 K for all 22 ATMS channels and the 4 RCs. The values derived from our analysis, which is labeled as STAR (i.e., the Center for Satellite Applications and Research), are consistent with those derived from the Northrop Grumman Electronic Systems (NGES) analysis. Table 4 lists the nonlinearity values at other cold plate temperatures from four RCs (also, see the *NGES Technique Report 14029B*, 2007).

[14] In the ATMS TDR processing algorithm, the blackbody brightness temperature, $T_{b,ch}^w$, is determined from its physical (or kinetic) temperature measured by the embedded platinum resistance thermometers (PRTs). The blackbody and cold space calibration counts, C_w and C_c, are averaged over several calibration cycles before being used in equation (2c) to obtain the calibrated gain.

[15] The ith channel cold space brightness temperature, $T_{b,ch}^c$ ($ch = 1, \ldots, 22$), is estimated by adding two correction terms to the cold space temperature, T^c. The first correction term, $\Delta T_{b,i}^{c,SL}$, takes into account the Earth radiation into the antenna side lobes and the second correction term, $\Delta T_{b,ch}^{c,RJ}$,

corrects the error introduced by the Rayleigh-Jeans (RJ) approximation. Specifically, $T_{b,ch}^c$ is written as

$$T_{b,ch}^c = T^c + \Delta T_{b,ch}^{c,SL} + \Delta T_{b,ch}^{c,RJ} \qquad (5)$$

[16] Details on these two correction terms can be found in *Weng et al.* [2012] and *Weng and Zou* [2013].

[17] The averaged warm load temperature for the ith scan is determined from the multiple PRT temperatures $T^w(k,j)$
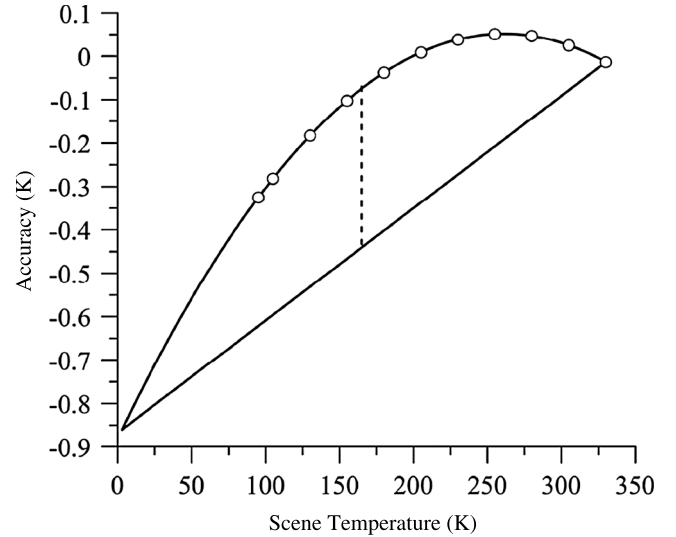

Figure 5. Nonlinearity of ATMS channel 1, calculated for cold plate (CP) at 5°C for redundancy configuration 1 (RC1). The data from the thermal vacuum experiments are shown as circles on the curve. Black solid curve represents the regression curve. Dashed line represents the peak nonlinearity.

Table 3. The Peak Nonlinearity Values for All 22 Channels for CP RC1, RC2, RC5, and RC6 at +5°C, Obtained From a Temperature Range of 3–276 K

Chan.	RC1		RC2		RC5		RC6	
	NGES	STAR	NGES	STAR	NGES	STAR	NGES	STAR
1	0.2553	0.2554	0.2758	0.2760	0.2813	0.2815	0.2869	0.2873
2	0.1287	0.1289	0.1505	0.1508	0.1504	0.1509	0.1543	0.1547
3	0.2012	0.2011	0.2143	0.2143	0.2478	0.2480	0.1938	0.1941
4	0.2758	0.2760	0.2832	0.2835	0.2627	0.2627	0.2702	0.2706
5	0.2720	0.2722	0.2925	0.2925	0.2888	0.2891	0.2739	0.2741
6	0.1438	0.1442	0.1723	0.1728	0.1994	0.1999	0.1956	0.1961
7	0.1463	0.1462	0.1552	0.1554	0.1422	0.1422	0.1468	0.1471
8	0.2553	0.2554	0.2627	0.2628	0.2758	0.2758	0.2590	0.2590
9	0.0417	0.0420	0.0585	0.0586	0.0794	0.0792	0.0688	0.0690
10	0.2664	0.2668	0.2254	0.2257	0.2199	0.2202	0.2236	0.2241
11	0.2329	0.2330	0.2776	0.2778	0.3391	0.3395	0.3018	0.3020
12	0.2385	0.2385	0.2068	0.2069	0.2404	0.2402	0.2385	0.2385
13	0.2087	0.2085	0.1563	0.1572	0.1789	0.1787	0.1504	0.1502
14	0.0904	0.0916	0.0922	0.0931	0.1645	0.1640	0.1323	0.1329
15	0.1722	0.1733	0.2310	0.2316	0.2832	0.2818	0.3130	0.3144
16	0.3335	0.3327	0.3484	0.3474	0.3335	0.3328	0.3354	0.3340
17	0.3875	0.3861	0.3559	0.3547	0.3875	0.3870	0.3428	0.3421
18	0.2981	0.2969	0.3112	0.3097	0.3037	0.3029	0.2832	0.2817
19	0.3093	0.3081	0.3074	0.3064	0.3261	0.3246	0.3130	0.3115
20	0.3652	0.3634	0.3447	0.3431	0.3298	0.3291	0.3372	0.3357
21	0.3093	0.3067	0.2813	0.2793	0.3037	0.3021	0.3205	0.3184
22	0.3633	0.3614	0.3018	0.3008	0.3540	0.3525	0.3633	0.3615

$(k = i - N_s, \ldots, i + N_s; j = 1, \ldots, N_p)$. Depending on user's need, a temperature-dependent bias correction from either ATMS telemetry file (i.e., $\Delta T^{shelf}_{w,ch}$) or user-defined values can be applied via equation (6).

$$\overline{T^w_{ch}}(i) = \frac{\sum\limits_{k=i-N_s}^{i+N_s} \sum\limits_{j=1}^{N_p} W_{k,j} T^w(k,j)}{\sum\limits_{k=i-N_s}^{i+N_s} \sum\limits_{j=1}^{N_p} W_{k,j}} + \Delta T^{shelf}_{w,ch} \qquad (6)$$

where $T^w(k,j)$ is the jth PRT temperature for the kth scan; $\Delta T^{shelf}_{w,ch}$ is the energy contributed from the channel-dependent receiving shelf temperature, and $W_{i,j}$ is the weighting coefficient. If a PRT is deemed to be bad by user, it is then excluded from the calibration process and the corresponding weighting coefficient is set to zero in the parameter file. Values of $\Delta T^{shelf}_{w,ch}$ are provided in Table 7. Theoretically, the warm load temperature also needs to be adjusted for the error introduced by Rayleigh-Jeans' approximation, i.e.,

$$T^w_{b,i} = T^w_{ch} + \Delta T^{w,RJ}_{b,ch} \qquad (7)$$

[18] Since the warm load temperature is normally operating above 280 K, the errors are typically negligible at lower ATMS frequencies [*Weng and Zou*, 2013].

4. ATMS Sensitivity

[19] The noise equivalent delta temperature (NEDT) for a specified channel describes the precision of measured radiances or brightness temperatures at the observing frequency. It is determined by computing the standard deviation of the

brightness temperature of the warm calibration target, $T^w_{b,ch}(i,j)$ as

$$\mathrm{NEDT}_{ch} \equiv \sigma^2\left(T^w_{b,ch}\right) \qquad (8)$$

where $T^w_{b,ch}(i,j)$ is related to the warm count, $C^w_{ch}(i,j)$ from the previously introduced linear calibration algorithm:

$$T^w_{b,ch} = \overline{T^w_{b,ch}} + \left(\overline{G_{ch}}\right)^{-1}\left(C^w_{ch} - \overline{C^w_{ch}}\right) \qquad (9)$$

[20] Substituting equation (9) into equation (8) results in the following expression for computing NEDT at each ATMS channel from the recorded multiple readings of ATMS radiometric count and the gain function:

$$\mathrm{NEDT}_{ch} = \left[\frac{1}{4N}\sum_{i=1}^{N}\sum_{j=1}^{4}\left(\frac{C^w_{ch}(i,j) - \overline{C^w_{ch}}(i)}{\overline{G_{ch}}(i)}\right)^2\right]^{1/2} \qquad (10)$$

[21] The first summation in equation (10) represents an averaged deviation (by a factor of 4) of the four warm calibration measurements at the ith scan line and the second summation represents an average over a total of N scan lines. The mean warm counts and mean calibration gain are computed using equations (2a) and (2c), respectively.

[22] The standard deviation quantifies the spread of the statistical distribution of the measuring values around the mean. However, it is not always an appropriate parameter for describing a spread of the statistical distribution of the measuring values around the mean that is nonstationary. The ATMS warm calibration counts are subject to considerable long-term variations due largely to temperature-dependent instrument gain variations; these variations are removed by on-orbit calibration, and therefore do not contribute to actual radiometric sensitivity (i.e., NEDT). Therefore, to

Table 4. The Peak Nonlinearity Values for All 22 Channels for CP RC1, RC2, RC5, and RC6 at (a) −10°C, (b) +5°C, and (c) +20°C, Given by the NGES Technique Report 14029B

|	NGES Technique Report 14029B			
Chan.	RC1	RC2	RC5	RC6
	(a) at −10°C			
1	0.2270	0.2340	0.2230	0.2190
2	−0.0200	−0.0260	−0.0190	−0.0280
3	0.1610	0.1630	0.1820	0.1660
4	0.2150	0.2220	0.2090	0.2140
5	0.2150	0.2150	0.2210	0.2140
6	0.1240	0.1490	0.1470	0.1290
7	0.1350	0.1270	0.1220	0.1440
8	0.2160	0.2220	0.2300	0.2280
9	0.0200	0.0500	0.0660	0.0580
10	0.1560	0.1620	0.1580	0.1770
11	0.2380	0.1940	0.2030	0.1770
12	0.1630	0.1290	0.1570	0.1920
13	0.1030	0.0300	0.0630	0.0790
14	0.0510	−0.0050	0.0080	0.0480
15	0.1180	0.2370	0.1770	0.2080
16	0.3400	0.3330	0.3330	0.3440
17	0.3870	0.3460	0.3820	0.3560
18	0.2940	0.3380	0.3060	0.2890
19	0.3040	0.3450	0.3330	0.2940
20	0.3500	0.3480	0.3620	0.3250
21	0.3090	0.3460	0.3350	0.3150
22	0.4040	0.4020	0.3910	0.3270
	(b) at +5°C			
1	0.2540	0.2740	0.2800	0.2870
2	0.1280	0.1500	0.1500	0.1540
3	0.2000	0.2130	0.2470	0.1930
4	0.2750	0.2820	0.2610	0.2700
5	0.2710	0.2910	0.2880	0.2730
6	0.1430	0.1720	0.1990	0.1950
7	0.1460	0.1550	0.1420	0.1460
8	0.2540	0.2620	0.2750	0.2580
9	0.0420	0.0580	0.0790	0.0690
10	0.2650	0.2250	0.2200	0.2220
11	0.2330	0.2760	0.3390	0.3000
12	0.2380	0.2060	0.2390	0.2380
13	0.2080	0.1560	0.1780	0.1500
14	0.0900	0.0920	0.1640	0.1320
15	0.1720	0.2290	0.2820	0.3120
16	0.3330	0.3470	0.3330	0.3350
17	0.3870	0.3550	0.3860	0.3420
18	0.2980	0.3100	0.3020	0.2830
19	0.3080	0.3050	0.3250	0.3120
20	0.3640	0.3440	0.3280	0.3360
21	0.3080	0.2790	0.3030	0.3190
22	0.3620	0.3000	0.3520	0.3620
	(c) at +20°C			
1	0.3540	0.3520	0.3570	0.3470
2	0.5320	0.5330	0.5610	0.5540
3	0.2590	0.2950	0.2690	0.2800
4	0.3290	0.3170	0.3340	0.3270
5	0.3230	0.3350	0.3390	0.3320
6	0.2370	0.2210	0.2410	0.2080
7	0.1720	0.2000	0.1920	0.1870
8	0.3180	0.3380	0.3300	0.2990
9	0.1080	0.1140	0.0940	0.0910
10	0.2770	0.2870	0.3090	0.3030
11	0.3400	0.3250	0.3130	0.3290
12	0.2840	0.2720	0.3210	0.2890
13	0.1990	0.2820	0.2200	0.1750
14	0.1700	0.1160	0.1800	0.2010
15	0.1840	0.5440	0.4050	0.2350
16	0.4060	0.4060	0.3890	0.3990
17	0.4720	0.4400	0.4400	0.4160
18	0.3080	0.3530	0.3010	0.3400
19	0.3670	0.3250	0.3250	0.3680
20	0.4170	0.3350	0.3900	0.3530
21	0.3720	0.3790	0.4020	0.3330
22	0.4250	0.4250	0.3760	0.4090
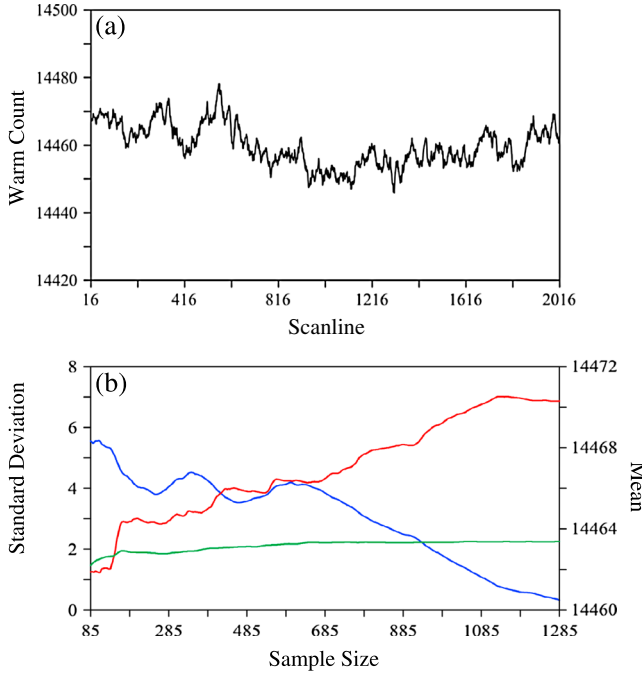
Figure 6. (a) Variations of the along-track 17-scanline averaged warm count of ATMS channel 1 on the first ATMS swath on 24 February 2012. (b) Variation of the mean (blue, *y* axis on the right) and the standard deviation (red, *y* axis on the left) and the overlapping Allan deviation (green, *y* axis on the left) of the 17-scanline averaged warm counts with sample size.

better describe the precision of ATMS radiances or brightness temperatures at the observed frequency, we use the so-called Allan deviation [*Allan*, 1987; *Allan et al.*, 1997] , which is defined as follows:

$$\sigma^{Allan}(m) = \sqrt{\frac{1}{2m^2(N-2m)} \sum_{j=1}^{N-2m} \left(\sum_{i=j}^{j+m-1} \left(C_{ch}^w(i+m) - C_{ch}^w(i) \right) \right)^2} \tag{11}$$

where *N* is the total number of data and *m* is the number of samples.

[23] Figure 6 presents the variations of the along-track averaged warm counts of ATMS channel 1 from an ATMS orbit data on 24 February 2012 (Figure 6a), as well as the variations of the mean, the standard deviation, and the Allan deviation of the warm counts versus a large range of sample size (Figure 6b). As seen in Figure 6b, the mean is not stationary and it decreases as the sample size increases. The standard deviation is also not stationary but it increases as the sample size increases. However, it is clear that the Allan deviation is much more stable over the whole range of sample size, which makes the Allan deviation more objective, thus a more proper measure to the ATMS channel precision.

[24] Figure 7 compares the NEDT values from equation (10) and the Allan deviation from equation (11). Both equations average data of 17 scan lines. It is noticed that the NEDT values (blue) for all ATMS channels are about 3–5

times larger than the Allan deviations (red). This is because the standard deviation used to quantify the sensitivity around the mean is not stationary. One related issue is that although the noises in ATMS measured brightness temperatures are well within the specification, the impact of the flicker noise shown in the measurements cannot be neglected. Mitigation of the flicker noise requires a significant effort and is beyond the scope of this paper. Since the launch of SNPP, ATMS NEDT is under monitoring, and is very stable and within specification (http://www.star. nesdis.noaa.gov/icvs/NPP/ipm_telemetry_npp_atms.php). The ATMS NEDT values are generally higher than the corresponding AMSU-A values mainly because the ATMS integration time is much shorter than that of AMSU-A [*Weng et al.*, 2013]. Specifically, the ATMS integration time for all ATMS channels is about 18 ms while that for AMSU-A channels 1–2 and 3–15 are 165 ms and 158 ms, respectively. Thus, when averaged for equivalent sampling intervals, the sensitivity performance of ATMS is better than that for AMSU-A [*Zou et al.*, 2013].

5. ATMS TDR to SDR Algorithm

[25] For a cross-track scanning microwave radiometer, pure vertical (V) or horizontal (H) polarization measurements only occur at the nadir direction. At the other scan angles, the measurements represent a mixed contribution from both V and H polarizations. Thus, it is necessary to define the quasi-vertical and quasi-horizontal antenna brightness temperatures (TDR), T_a^{Qv} and T_a^{Qh}, via [*Bormann et al.*, 2013] the following:

$$T_a^{Qv} = \eta_{me}^{vv} T_b^{Qv} + \eta_{me}^{hv} T_b^{Qh} + \eta_{se}^{vv} T_{b,se}^{Qv} + \eta_{se}^{hv} T_{b,se}^{Qh}$$
$$+ \left(\eta_{sc}^{vv} + \eta_{sc}^{hv} \right) T_{c,RJ} + S_a^{Qv} \tag{12a}$$

$$T_a^{Qh} = \eta_{me}^{hh} T_b^{Qh} + \eta_{me}^{vh} T_b^{Qv} + \eta_{se}^{hh} T_{b,se}^{Qh} + \eta_{se}^{vh} T_{b,se}^{Qv}$$
$$+ \left(\eta_{sc}^{hh} + \eta_{sc}^{vh} \right) T_{c,RJ} + S_a^{Qh} \tag{12b}$$

where η_{me}^{vv} and η_{me}^{hh} are the copolarized antenna main beam efficiencies; η_{me}^{vh} and η_{me}^{hv} are the cross-polarized antenna main beam efficiencies; $\left(\eta_{se}^{vv}, \eta_{se}^{hh} \right)$ and $\left(\eta_{se}^{vh}, \eta_{se}^{hv} \right)$ are the copolarized and cross-polarized antenna sidelobe beam efficiencies, respectively; and $\left(\eta_{sc}^{vv}, \eta_{sc}^{hh} \right)$ and $\left(\eta_{sc}^{vh}, \eta_{sc}^{hv} \right)$ are
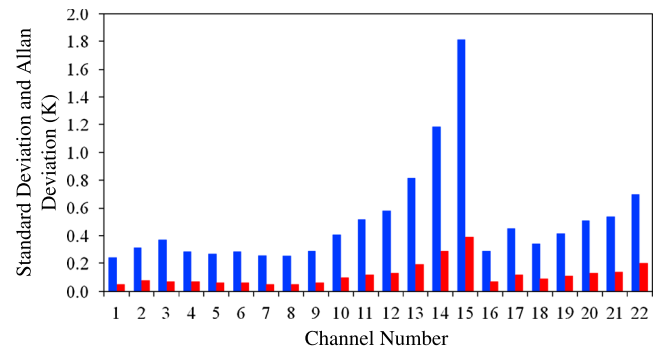

Figure 7. Variations of NEDT and Allan deviation with channel number. The sample size (*N*) is 150 and the averaging factor (*m*) for the warm counts is 17. NEDT values (standard deviation, blue); Allan deviation (red).

Table 5. ATMS Antenna Main Beam Efficiencies Analyzed From Copolarization and Cross-Polarization Antenna Gain Distribution Functions

	η_{me}^{pp} (%)			η_{me}^{pq} (%)		
Channel	B1	B48	B96	B01	B48	B96
1	95.5	95.3	95.9	0.84	0.73	0.81
2	97.0	96.4	96.8	0.64	0.65	0.64
3	96.2	95.6	96.3	1.01	1.05	0.90
4	96.2	95.7	96.6	0.95	0.94	0.70
5	96.2	95.8	96.1	0.87	0.91	0.98
6	96.3	95.9	96.2	0.88	0.94	1.04
7	96.5	96.1	96.6	0.87	0.86	0.82
8	96.6	96.1	96.2	0.90	0.90	1.13
9	96.7	96.2	96.6	0.90	0.88	0.86
10	97.3	97.1	97.2	0.92	0.91	0.93
11	97.3	97.1	97.2	0.92	0.91	0.93
12	97.3	97.1	97.2	0.92	0.91	0.93
13	97.3	97.1	97.2	0.92	0.91	0.93
14	97.3	97.1	97.2	0.92	0.91	0.93
15	97.3	97.1	97.2	0.92	0.91	0.93
16	90.9	91.3	91.7	4.71	4.65	4.54
17	86.2	83.9	86.6	3.71	3.40	5.18
18	86.5	85.2	85.2	3.31	3.46	5.12
19	86.0	87.4	89.3	4.03	2.25	1.85
20	86.0	87.4	89.3	4.03	2.25	1.85
21	86.0	87.4	89.3	4.03	2.25	1.85
22	86.0	87.4	89.3	4.03	2.25	1.85

the cold space copolarized and cross-polarized sidelobe beam efficiencies. It is worth pointing out that each ATMS frequency channel only measures one single polarization, i.e., either horizontal or vertical (listed in Table 1). Therefore, in equations (12a) and (12b) there are, correspondingly, only one copolarization and one cross-polarization antenna beam efficiencies in pair for each of the antenna main beam, antenna sidelobe, and cold space sidelobe. Values of all the beam efficiencies are summarized in Tables 5, 6, and 7.

[26] The quasi-vertical and quasi-horizontal sensor brightness temperatures, T_b^{Qv} and T_b^{Qh}, are related to the pure vertically and horizontally polarized brightness temperatures, T_b^v and T_b^h, through the following relationships:

$$T_b^{Qv} = T_b^v \cos^2\theta + T_b^h \sin^2\theta \qquad (13a)$$

$$T_b^{Qh} = T_b^v \sin^2\theta + T_b^h \cos^2\theta \qquad (13b)$$

where θ is the scan angle. From equations (13a) and (13b), it is easy to see that both T_b^{Qv} and T_b^{Qh} vary with scan angle and are the same at the nadir and 45° scan angle.

[27] Polarization difference is only significant over an ocean surface. Figure 8 shows an example of the brightness temperatures estimated from both pure polarization and quasi-polarization at the selected ATMS channels. As shown in Figure 8, for all channels the brightness temperature differences between quasi-vertical and quasi-horizontal polarizations are correspondingly smaller than their counterparts from the pure polarizations.

[28] The last terms in equations (12a) and (12b), S_b^{Qv} and S_b^{Qh}, are considered as the radiation contributions from the antenna near-field sidelobe or other effects such as the emitted radiation from ATMS flat reflector (see E. Kim et al., submitted manuscript, 2013), and can be estimated from the ATMS

pitch-maneuver data [*Weng et al.*, 2013]. Using the ATMS pitch-maneuver data, the following relationships are derived:

$$S_a^{Qv} = \beta_0^v + \beta_1^v \sin^2\theta \qquad (14a)$$

$$S_a^{Qh} = \beta_0^h + \beta_1^h \cos^2\theta \qquad (14b)$$

where β_k^v and β_k^h ($k = 0, 1$) are the coefficients obtained by fitting the ATMS data during its pitch-maneuver period on 20 February 2012 [*Weng et al.*, 2013], provided in Table 7. The antenna beam efficiencies for all ATMS channels are also listed in Table 7 as reference. For channels 16–22, the beam efficiencies have large uncertainties because of the high measurement noise level in the data sets. The values listed in Tables 5, 6, and 7 are derived without cutting the noise level in the ATMS antenna gain distribution data sets.

[29] Assuming $T_{b,se}^{Qv} \approx T_b^{Qv}$ and $T_{b,se}^{Qh} \approx T_b^{Qh}$, equations (12a) and (12b) can be rewritten as

$$T_a^{Qv} = \left(\eta_{me}^{vv} + \eta_{se}^{vv}\right)T_b^{Qv} + \left(\eta_{me}^{hv} + \eta_{se}^{hv}\right)T_b^{Qh}$$
$$+ \left(\eta_{sc}^{vv} + \eta_{sc}^{hv}\right)T_{c,RJ} + S_a^{Qv} \qquad (15a)$$

$$T_a^{Qh} = \left(\eta_{me}^{hh} + \eta_{se}^{hh}\right)T_b^{Qh} + \left(\eta_{me}^{vh} + \eta_{se}^{vh}\right)T_b^{Qv}$$
$$+ \left(\eta_{sc}^{hh} + \eta_{sc}^{vh}\right)T_{c,RJ} + S_a^{Qh} \qquad (15b)$$

[30] For a fixed scan angle and a given surface condition, T_b^{Qv} and T_b^{Qh} are related to each other via the following empirical models:

$$T_b^{Qh} = A^h(\theta) T_b^{Qv}$$

$$T_b^{Qv} = A^v(\theta) T_b^{Qh}$$

where $A^h(\theta)$ and $A^v(\theta)$ are functions depending on the scan angle. At scan angles of 0° and 45°, and for the channels that are not

Table 6. ATMS Antenna Sidelobe Earth Beam Efficiencies Analyzed From Copolarization and Cross-Polarization Antenna Gain Distribution Functions

	η_{se}^{pp} (%)			η_{se}^{pq} (%)		
Channel	B1	B48	B96	B01	B48	B96
1	2.30	3.10	2.01	0.56	0.54	0.35
2	1.55	2.25	1.53	0.35	0.37	0.22
3	1.71	2.46	1.74	0.45	0.51	0.44
4	1.93	2.49	1.83	0.43	0.45	0.33
5	1.86	2.40	1.80	0.47	0.50	0.39
6	1.75	2.32	1.72	0.44	0.51	0.44
7	1.66	2.21	1.66	0.44	0.43	0.32
8	1.62	2.11	1.54	0.37	0.46	0.45
9	1.63	2.13	1.61	0.33	0.41	0.34
10	1.18	1.47	1.12	0.27	0.28	0.26
11	1.18	1.47	1.12	0.27	0.28	0.26
12	1.18	1.47	1.12	0.27	0.28	0.26
13	1.18	1.47	1.12	0.27	0.28	0.26
14	1.18	1.47	1.12	0.27	0.28	0.26
15	1.18	1.47	1.12	0.27	0.28	0.26
16	1.34	2.12	1.45	1.33	1.36	0.87
17	3.83	5.68	3.49	1.73	1.83	1.66
18	5.10	5.30	4.80	1.41	1.59	1.51
19	5.10	5.30	4.80	1.41	1.59	1.51
20	5.17	5.37	5.01	1.44	1.37	0.95
21	5.17	5.37	5.01	1.44	1.37	0.95
22	5.17	5.37	5.01	1.44	1.37	0.95

Table 7. ATMS Antenna Sidelobe Cold Space Efficiencies Analyzed From Copolarization and Cross-Polarization Antenna Gain Distribution Functions During SNPP ATMS Thermal Vacuum Tests[a]

Channel	$\eta_{sc}^{pp} + \eta_{sc}^{pq}$ (%)			$\Delta T_{b,ch}^{c,RJ}$	$\Delta T_{b,ch}^{c,SL}$	ΔT_{ch}^{w}	β_0	β_1
	B1	B48	B96					
1	0.78	0.29	0.95	0.034	0.398	0.045999	0.0553	0.8123
2	0.49	0.36	0.76	0.166	0.528	0.075999	0.0389	0.7167
3	0.60	0.38	0.58	0.176	0.220	0.074999	0.0460	0.3781
4	0.52	0.42	0.57	0.183	0.206	0.086999	−0.0010	0.4499
5	0.56	0.44	0.72	0.189	0.220	0.083000	0.0527	0.3877
6	0.60	0.35	0.63	0.194	0.206	0.085999	0.0144	0.4520
7	0.52	0.41	0.61	0.198	0.220	0.088999	0.0730	0.4503
8	0.53	0.40	0.66	0.202	0.249	0.087999	0.1133	0.4517
9	0.46	0.34	0.55	0.216	0.233	0.075999	0.1049	0.4558
10	0.35	0.22	0.48	0.216	0.233	0.085000	0.1419	0.5474
11	0.35	0.22	0.48	0.216	0.206	0.084000	0.1271	0.5199
12	0.35	0.22	0.48	0.216	0.206	0.087999	0.1675	0.4969
13	0.35	0.22	0.48	0.216	0.206	0.060999	0.1190	0.5213
14	0.35	0.22	0.48	0.216	0.206	0.010400	0.1187	0.5283
15	0.35	0.22	0.48	0.216	0.206	0.042000	0.1583	0.6107
16	1.70	0.53	1.40	0.506	0.610	0.015900	0.0065	1.1983
17	4.53	5.23	3.08	1.638	0.102	0.015500	−0.0697	0.7106
18	3.69	4.42	3.36	1.959	0.126	0.015300	−0.1200	0.9832
19	3.69	4.42	3.36	1.959	0.126	0.014699	−0.0623	0.8911
20	3.41	3.59	2.89	1.959	0.126	0.015100	−0.0525	0.8986
21	3.41	3.59	2.89	1.959	0.126	0.014399	−0.0147	0.8773
22	3.41	3.59	2.89	1.959	0.126	0.016000	−0.0689	1.0274

[a]Cold space temperature is 2.73 K and the correction to the cold space temperature from uses of RJ approximation and the contributions to RJ cold space temperature from the sidelobe of the earth are shown. ($pp = vv,hh$; $pq = vh,hv$; $T_{c,RJ} = 2.73 + \Delta T_{c,RJ}$).

impacted by the surface polarization, $A^h(\theta) = 1$ and $A^v(\theta) = 1$. Thus, equations (15a) and (15b) can be further written as

$$T_a^{Qv} = \left[\left(\eta_{me}^{vv} + \eta_{se}^{vv}\right) + A^v\left(\eta_{me}^{hv} + \eta_{se}^{hv}\right)\right]T_b^{Qv} + \left(\eta_{sc}^{vv} + \eta_{sc}^{hv}\right)T_{c,RJ} + S_a^{Qv} \quad (16a)$$

$$T_a^{Qh} = \left[\left(\eta_{me}^{hh} + \eta_{se}^{hh}\right) + A^h\left(\eta_{me}^{vh} + \eta_{se}^{vh}\right)\right]T_b^{Qh} + \left(\eta_{sc}^{hh} + \eta_{sc}^{vh}\right)T_{c,RJ} + S_a^{Qh} \quad (16b)$$

[31] Tables 5, 6, and 7 list all the coefficients needed for the above conversion between antenna temperatures (TDR) and brightness temperatures (SDR). Note that ATMS channels 1–3 and 16 have 1 to 4% polarization spillover radiation. Thus, a correction must be made to account for the contribution of polarization spillover effect between TDR and SDR conversions. Moreover, for ATMS W and G bands (channels 16–22), the beam efficiencies listed in the tables remain highly uncertain. The ATMS vendor, NGES, has provided the W and G band beam efficiencies; however, the results have not been verified by others. Further investigation on this issue is required. Thus, for ATMS W and G bands, the current TDR data are only corrected for the near-field sidelobe contributions for the SDR data by setting the antenna main beam efficiency to 1.

[32] For ATMS channels 1, 2, and 16, TDRs are converted to SDRs using the following equation:

$$T_b^{Qv} = \left[T_a^{Qv} - \left(\eta_{sc}^{vv} + \eta_{sc}^{hv}\right)T_{c,RJ} - S_a^{Qv}\right] / \left[\eta_{me}^{vv} + \eta_{se}^{vv} + A^v\left(\eta_{me}^{hv} + \eta_{se}^{hv}\right)\right] \quad (17a)$$

[33] For the other ATMS channels,

$$T_b^{Qh} = \left[T_a^{Qh} - \left(\eta_{sc}^{hh} + \eta_{sc}^{vh}\right)T_{c,RJ} - S_a^{Qh}\right] / \left[\eta_{me}^{hh} + \eta_{se}^{hh} + A^h\left(\eta_{me}^{vh} + \eta_{se}^{vh}\right)\right] \quad (17b)$$

6. SDR Assessment

[34] The above ATMS TDR to SDR conversion algorithm is tested by comparing the ATMS SDR products (O) with the corresponding NWP CRTM simulation results (B) using either the NCEP GFS 6 h forecasts or GPS RO data as inputs. The first O-B comparison is shown in Figure 9. In this comparison, the NCEP GFS forecast fields include 64 layers from surface to about 0.1 hPa. The CRTM simulations during the period of 20–26 December 2011 are averaged from all the data over the ocean surfaces. For ATMS channels 2 and 8, only those data sets with cloud liquid water path (LWP) being less than 0.03 kg/m², (total precipitable water) TPW being less than 10 kg/m², and surface wind speed being less than 7 m/s are analyzed. For ATMS channels 16 and 20, cloud LWP is less than 0.03 kg/m² and surface wind speed is less than 7 m/s. Overall, as seen in Figure 9, the ATMS observations compared quite favorably with model simulations, especially for the temperature-sounding channel (channel 8). Possible reasons for the wider spread shown in the other three channels may be (1) cloud impacts (i.e., some clouds may still exist even after applying the above quality control) and (2) model uncertainties, especially for the water vapor sounding channels (i.e., channel 20).

[35] ATMS observations are also compared with the simulations with GPS RO profiles as input to CRTM. Since the geolocation of the perigee point (also called tangent point) of a single RO profile varies with altitude, the collocation between ATMS observations and GPS RO are performed at each perigee point. On the other hand, a satellite measurement at a specific frequency represents a weighted average of radiation emitted from different layers of the atmosphere. The measured radiation is most sensitive to the atmospheric temperature at the altitude where the weighting function (WF) reaches a maximum [Zou et al., 2013]. For each channel, the altitude of the peak WF
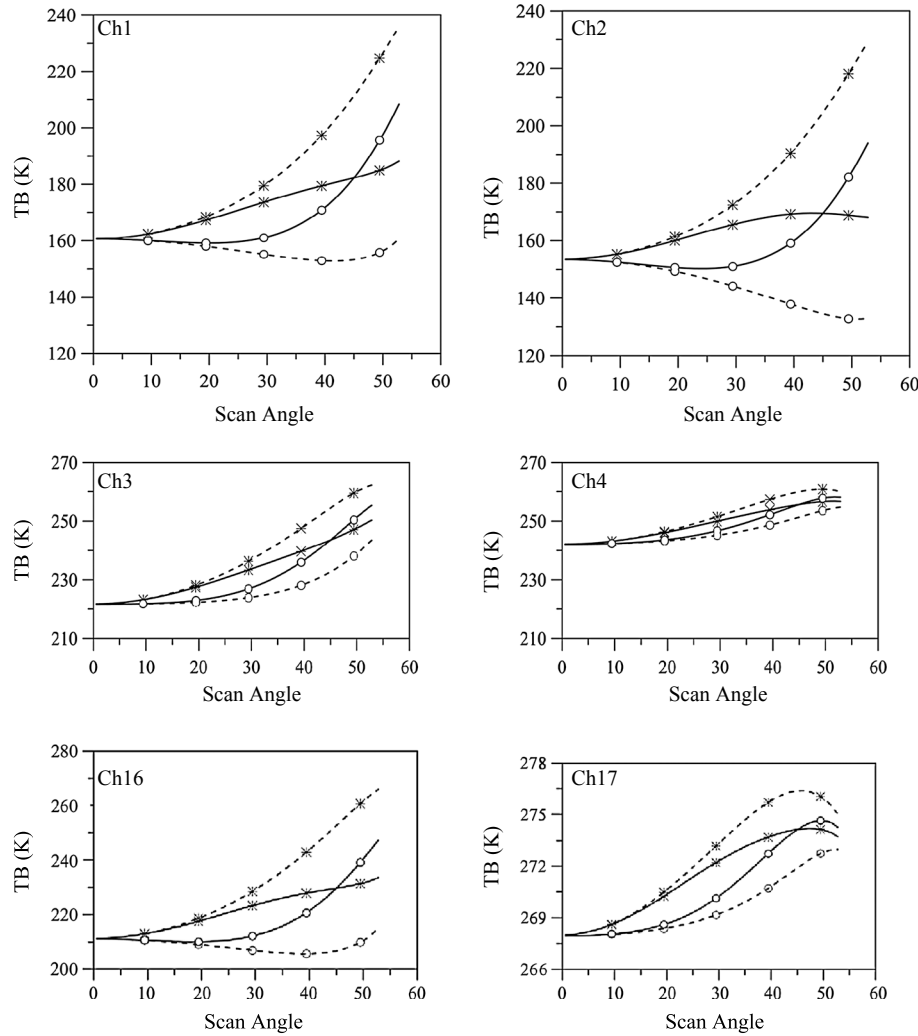
Figure 8. The brightness temperature with pure (dashed curve) and quasi- (solid curve) horizontal polarization (circle) and vertical (star) polarization states using the U.S/ standard atmospheric profile with sea surface wind speed being 5 m/s and sea surface temperature being 290 K.

is lowest at the nadir and increases with the scan angle. Considering the geolocation change of the perigee point of a GPS RO profile with altitude, the geolocation of a GPS RO is used to match the altitude at which the ATMS WF at a channel reaches the maximum. The spatial difference between ATMS and GPS RO is less than 50 km. The altitude of the maximum WF is determined by inputting the U.S. standard atmosphere profile into CRTM (see Table 1).

[36] Besides a horizontal spatial separation of less than 30 km at the altitude of peak weighting function, the collocation criteria are set by a time difference of no more than half hour. If there are more than one ATMS pixel measurements satisfying these collocation criteria, the one that is closest to the related Constellation Observing System for Meteorology, Ionosphere and Climate (COSMIC) sounding is chosen and others are discarded. Because surface state variables and parameters are not provided by COSMIC ROs, only upper level temperature-sounding channels are simulated using COSMIC GPS RO data.

[37] ATMS observations are only compared with simulations under clear conditions. Over oceans, a cloud detection algorithm similar to *Weng et al.* [2003] is applied to

separate the data in clear-sky conditions over ocean from total ATMS measurements [*Weng et al.*, 2012]. Figure 10a presents the spatial distribution of the ATMS observations that are collocated with COSMIC GPS RO data in clear-sky conditions over ocean and between 60°S–60°N from 10 December 2011 to 31 March 2013. Less data are found in the tropics than in middle latitudes due to less GPS RO data. For GPS RO simulations, we only simulated ATMS SDR at channel 6 to 13 since the GPS RO profiles are most reliable with the midtroposphere to lower stratosphere. For channels 6–13, the mean biases between ATMS observations and GFS simulations, and those between ATMS observations and GPS RO simulations are positive and of similar magnitudes (Figure 10b). This consistency indicates that the ATMS SDR products perform well. Moreover, the standard deviations of the differences between ATMS observations and CRTM simulations with GFS 6 h forecasts are higher than the ATMS NEDT values (Figure 7) but smaller than those of the differences between ATMS observations and GPS RO simulations. It is worth mentioning that the standard deviations of the differences between ATMS observations and CRTM simulations with GFS 6 h
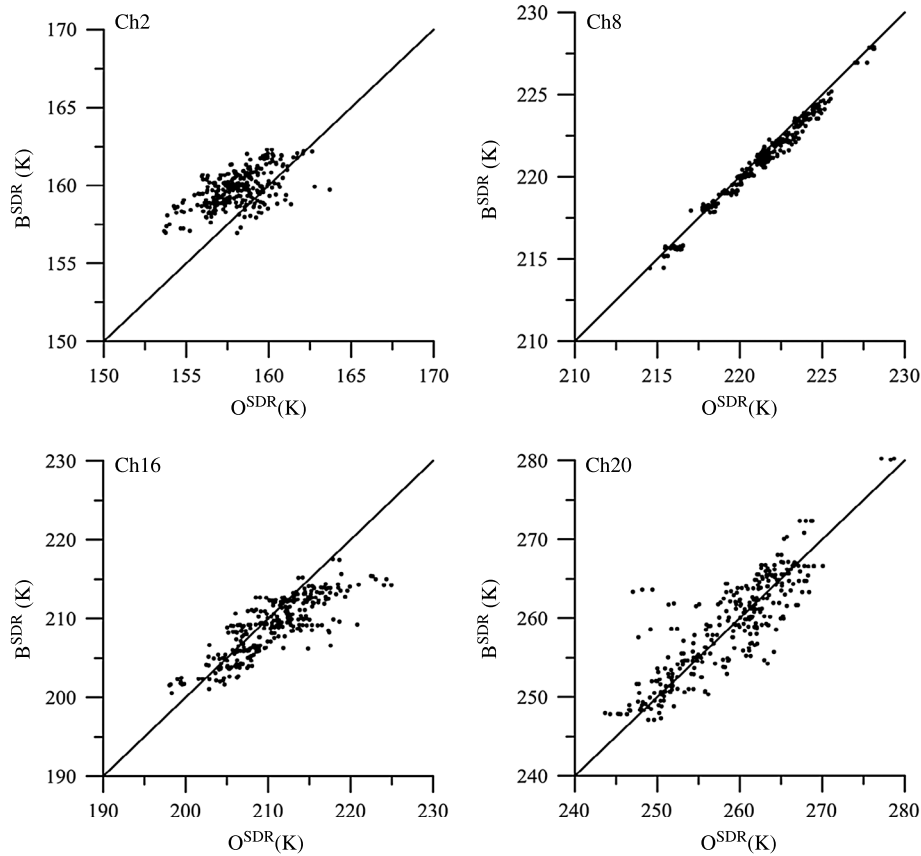
Figure 9. Scatterplots of ATMS SDR observations (O^{SDR}) and model simulation (B^{SDR}) for ATMS channels 2, 8, 16, and 20 over ocean under dry, clear-sky, and calm conditions using data during the period of 20–26 December 2011.

forecasts are much higher than the ATMS NEDT values for humidity channels and surface-sensitive channels. Accurate simulations of brightness temperatures for those surface-sensitive channels remain challenging due to the limited accuracy of the forward modeling components such as surface emissivity.

7. Summary and Conclusions

[38] Presented here is a thorough end-to-end ATMS calibration and validation study. In this paper, the ATMS Earth scene counts are calibrated to antenna brightness temperatures (TDR) through a two-point calibration algorithm with a quadratic nonlinear correction. The nonlinearity term is derived from the prelaunch TVAC data with a maximum value less than 0.5 K. After applying the nonlinear correction, the absolute accuracy of TDR for all ATMS channels is generally about 0.2 to 0.5 K, which meets the specification. Unlike AMSU-A/MHS calibration operating in radiance, ATMS calibration to TDR is directly carried out in brightness temperature based on the RJ approximation. Thus, the cold space temperatures are corrected to the apparent brightness temperatures prior to its use in the two-point calibration. In future, we plan to modify the current ground processing system into a full radiance space.

[39] The current algorithm for quantifying the precision of the ATMS radiometric measurements, NEDT, is described.

The NEDT values for all the channels are well within the instrument specification. However, through the sensitivity study of NEDT and the Allan deviation, we found that the Allan deviation may be a better metric for precision.

[40] Also, a new ATMS TDR to SDR algorithm is developed in this paper. This conversion is very important since SDR products can be directly used in the NWP models for satellite data assimilation. One thing needs to be pointed out: the convertibility is not always unique if ATMS antenna subsystem has a significant polarization spillover effect and/ or a sidelobe contribution from the nearby scene cells. While ATMS antenna gain distribution functions were measured during the prelaunch period, there remain some uncertainties in characterization of sidelobe and cross-polarization at high frequencies. At the conditions where ATMS brightness temperatures at quasi-vertical and quasi-horizontal polarization states are the same, the conversion from TDR to SDR becomes unique assuming all the sidelobe contributions are estimated. At 45° scan angle, ATMS SDR can be uniquely derived from its TDR and therefore directly compared with simulations. It is shown that the biases of ATMS SDRs with respect to GPS RO and GFS simulation are similar in magnitude. The largest biases are found for surface-sensitive channels at both low and high frequencies. Further investigation is planned to assess errors in the forward modeling associated with surface emissivity and surface parameters from GFS.
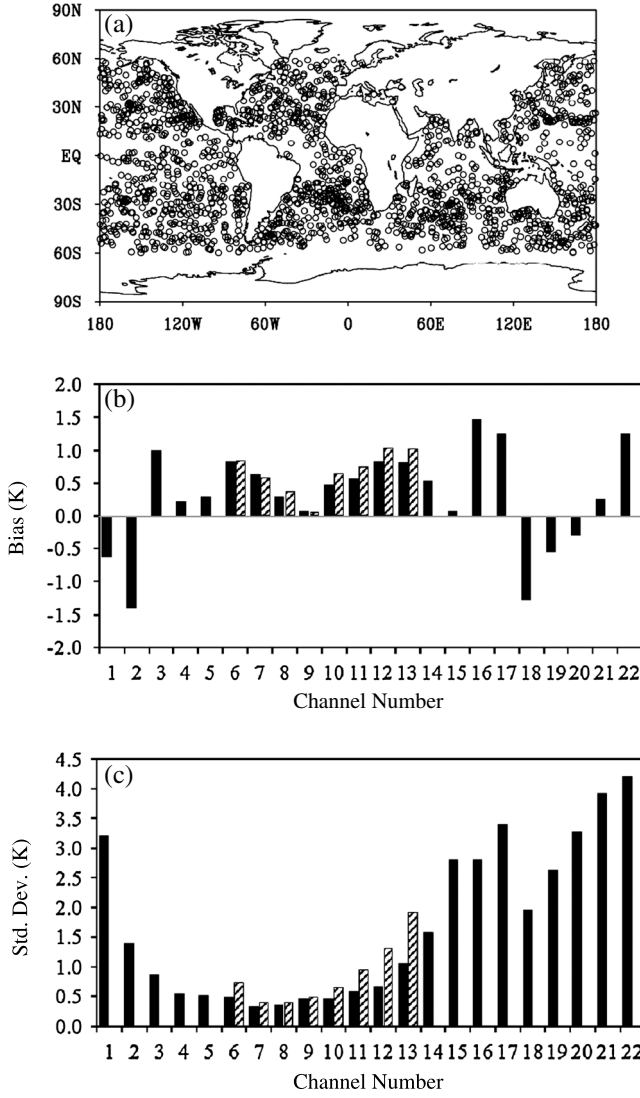
Figure 10. (a) Spatial distribution of ATMS measurements at 45° scan angle under clear-sky condition over ocean between 60°S and 60°N that are collocated with COSMIC RO profiles from 10 December 2011 to 31 March 2013. (b) Bias and (c) standard deviation of the differences between ATMS SDR observations and CRTM simulations with GFS 6 h forecasts (solid bar) and GPS RO profiles (dashed bar).

Appendix A: Conversion of Radiometric Calibration from Radiance to Brightness Temperature

[41] A radiometric calibration in radiance was derived as follows [*Mo*, 1999]:

$$R = R_w + (R_w - R_c)\left(\frac{C_s - \overline{C_w}}{\overline{C_w} - \overline{C_c}}\right) + Q \tag{A1}$$

$$Q = \mu(R_w - R_c)^2 \frac{(C_s - \overline{C_w})(C_s - \overline{C_c})}{(\overline{C_w} - \overline{C_c})^2} \tag{A2}$$

$$G = \frac{\overline{C_w} - \overline{C_c}}{R_w - R_c} \tag{A3}$$

$$\overline{C_x} = \sum_{i=-Ns}^{Ns} W_i C_x, x = w \text{ or } c \tag{A4}$$

[42] Here all variables in the equation should be channel specific. For simplicity, the channel subscript is omitted in all the following deviations. In the history of NOAA operational calibration, equation (A1) is expressed in a quadratic form

$$R = a_0 + a_1 C_s + a_2 C_s^2 \tag{A5}$$

[43] So the calibration coefficients, a_0, a_1, and a_2 can be expressed as follows:

$$a_0 = R_w - \frac{\overline{C_w}}{G} + \mu \frac{\overline{C_w C_c}}{G^2}, \tag{A6}$$

$$a_1 = \frac{1}{G} - \mu \frac{\overline{C_w} + \overline{C_c}}{G^2}, \tag{A7}$$

$$a_2 = \frac{\mu}{G^2}. \tag{A8}$$

[44] In the above radiometric calibration equations, the Earth scene counts are typically converted to the radiance. In general, the radiance describes the amount of electromagnetic energy radiated from an earth scene in a specified direction, a solid angle and a frequency interval. Thus, it can be computed by its kinetic temperature (T) and wave number (v)as follows:

$$R_v(T) = \frac{2hc^2 v^3}{\exp\left(\frac{hcv}{kT}\right) - 1} \equiv \frac{C_1 v^3}{\exp\left(\frac{C_2 v}{T}\right) - 1}, \tag{A9}$$

where k is the Boltzmann constant; h is the Planck constant; c is the speed of light (in m), $C_1 = 2hc^2 = 1.1909 \times 10^{-8}$ W m^{-2} sr^{-1} cm^{-1} cm^3, and $C_2 = \frac{hc}{k} = 1.438786$ cm K. Equation (A8) is known as the Planck radiation law.

[45] Assuming $\frac{C_2 v}{T} \ll 1$, the exponential function in Planck function can be expressed in Taylor series:

$$\exp\left(\frac{C_2 v}{T}\right) = 1 + \frac{C_2 v}{T} + \frac{1}{2}\left(\frac{C_2 v}{T}\right)^2 + \cdots + \frac{1}{n!}\left(\frac{C_2 v}{T}\right)^n + \cdots \tag{A10}$$

[46] Substituting the first-order approximation of the above Taylor expansion into equation A8 results in the following linear relationship between the blackbody temperature (T) and radiance (R_v)

$$R_v^{RJ}(T) = \frac{C_1 v^2}{C_2} T. \tag{A11}$$

[47] Equation (A10) is called the Rayleigh-Jeans (RJ) approximation to Planck's function. At the ATMS frequency range of 23.8 GHz $\leq f \leq$ 190.3 GHz), $C_2 v$ is generally less than 10 K, thus, the temperature in equation (A9) must be above 100 K. Substituting (A10) into equation (A1) results in

$$T_b = T_w (T_w - T_c)\left(\frac{C_s - \overline{C_w}}{\overline{C_w} - \overline{C_c}}\right) + Q_b, \tag{A12}$$

$$Q_b = \mu(T_w - T_c)^2 \frac{(C_s - \overline{C_w})(C_s - \overline{C_c})}{(\overline{C_w} - \overline{C_c})^2}. \tag{A13}$$

[48] The accuracy of the radiance calculated from RJ approximation varies with frequency and temperature. The radiometric calibration is processed through uses of equation (A12). As a result, the two-point calibration is derived in brightness temperature form as

$$T_b = T_w + {}^wG_b^{-1}\left(C_s - \overline{C_w}\right) + Q_b = T_{b,l} + Q_b \qquad (A14)$$

where the linear and nonlinear terms are expressed as

$$T_{b,l} = T_w + G_b^{-1}\left(C_s - \overline{C_w}\right), \qquad (A15)$$

$$Q_b = \mu G_b^{-2}\left(C_s - \overline{C_w}\right)\left(C_s - \overline{C_c}\right) = \mu(T_w - T_c)^2 x(1 - x), \quad (A16)$$

$$G_b = \frac{\overline{C_w} - \overline{C_c}}{T_w - T_c}, \qquad (A17)$$

respectively, where

$$x = \frac{T_{b,l} - T_c}{T_w - T_c}.$$

[49] The maximum nonlinearity value can be derived by performing the derivative with respect to x which is $f'(x) = 1 - 2x$. Using Taylor's expansion for $f(x) = x(1 - x)$ at $x_0 = 0.5$ which is equal to $C_s = 0.5\left(\overline{C_w} + \overline{C_c}\right)$, then

$$Q_b = \frac{1}{4}\mu(T_w - T_c)^2\left[1 - 4(x - 0.5)^2\right]$$
$$= Q^{\max}\left[1 - 4(x - 0.5)^2\right]. \qquad (A18)$$

If the first two terms in A15 are kept for the nonlinearity term, where

$$Q^{\max} = \frac{1}{4}\mu(T_w - T_c)^2. \qquad (A19)$$

References

Allan, D. W. (1987), Should the classical variance be used as a basic measure in standards metrology?, *IEEE Trans. Instrum. Meas.*, *IM-36*, 646–654.

Allan, D. W., N. Ashby, and C. C. Hodge (1997), The science of timekeeping, Appendix A. Hewlett Packard Application Note 1289, page 59.

Bormann, N., A. Fouilloux, and W. Bell (2013), Evaluation and assimilation of ATMS data in the ECMWF system, *ECMWF Technical Memoranda 689*, 1–41.

JPSS ATMS ATBD (2011), Joint Polar Satellite System (JPSS) Advanced Technology Microwave Sounder (ATMS) SDR Radiometric Calibration Algorithm Theoretical Basic Document (ATBD), http://www.star.nesdis.noaa.gov/jpss/documents/ATBD/GSFC_474-00043_JPSS_ATMS_SDR_Radiometric_Calibration_ATBD__Alt._doc._no._D43751_.pdf.

Mo, T. (1999), Calibration of the advanced microwave sounding unit-A radiometers for NOAA-L and NOAA-M. *NOAA Technical Report NESDIS*, 92, p. 53.

NGES technique report 14029B (2007), Advanced technology microwave sounder (ATMS) Calibration Data Book – ATMS PFM P/N 1362460–1 S/N 302.

Weng, F., L. Zhao, R. R. Ferraro, G. Poe, X. Li, and N. Grody (2003), Advanced microwave sounding unit cloud and precipitation algorithms, *Radio Sci.*, *38*(33), 1–12, doi:10.1029/2002RS002679.

Weng, F., X. Zou, X. Wang, S. Yang, and M. Goldberg (2012), Introduction to Suomi NPP ATMS for NWP and tropical cyclone applications, *J. Geophys. Res.*, *117*, D19112, doi:10.1029/2012JD018144.

Weng, F., and X. Zou (2013), Errors from Rayleigh-Jeans approximation in satellite microwave radiometer calibration system, *Appl. Optics*, *12*, 505–508.

Weng, F., H. Yang, and X. Zou (2013), On convertibility from antenna to sensor brightness temperature for advanced technology microwave sounder (ATMS), *IEEE Geosci. Remote. Sens. Letter*, doi:10.1109/LGRS.2012.2223193.

Zou, X., L. Lin, and F. Weng (2013), Absolute calibration of ATMS upper level temperature sounding channels using GPS RO observations, *IEEE Trans. Geosci. Remote. Sens.*, doi:10.1109/TGRS.2013.225098.